iR Drop in Scanning Electrochemical Cell Microscopy

Journal:	*Faraday Discussions*
Manuscript ID	FD-ART-07-2021-000046.R1
Article Type:	Paper
Date Submitted by the Author:	13-Aug-2021
Complete List of Authors:	Blount, Brandon; The University of Texas at Austin, Department of Chemistry Juarez, Gabriel; The University of Texas at Austin, Department of Chemistry Wang, Yufei; The University of Texas at Austin, Department of Chemistry Ren, Hang; The University of Texas at Austin, Department of Chemistry

iR Drop in Scanning Electrochemical Cell Microscopy

Brandon Blount[§], Gabriel Juarez[§], Yufei Wang, and Hang Ren*

Department of Chemistry, The University of Texas at Austin, 105 E 24th St, Austin, TX 78712.

Abstract

Nanoscale electrochemical mapping techniques, e.g., scanning electrochemical cell microscopy (SECCM), have been increasingly used to study the local electrochemistry in electrocatalysis. Its capability of local electrochemistry mapping helps to reveal the heterogeneity in the electrode kinetics and mechanisms which are otherwise averaged out in ensemble measurement. Accurate determination of the electrode kinetics requires careful assessment of the ohmic potential drop in the solution, i.e., *iR* drop. Herein, *iR* drop in SECCM experiments is assessed. We showed that *iR* drop in single-barrel SECCM can be estimated using the solution conductivity and the mass transfer limiting current without the assumption of pipette geometry. For dual-barrel SECCM, we developed a method of measuring the solution resistance directly, which can be used to compensate the *iR* drop and the potential shift in the experiments. These methods offer a convenient way to estimate and compensate the *iR* drop in SECCM, allowing more accurate measurement of local electrode kinetics for the determination of local mechanisms in electrocatalysis.

Introduction

Kinetic measurement of electrode processes plays an important role in the development of new electrocatalysts.[1, 2] Electrocatalytic mechanisms can often be inferred from the current-overpotential relationship, e.g., via Tafel analysis.[3] One good practice to ensure accurate measurement of electrode kinetics is to assess and compensate the ohmic drop between the working electrode and the reference electrode, i.e., *iR* drop.[4] The importance of *iR* drop in electrocatalysis has been recently re-emphasized, and failure to assess and compensate *iR* drop can lead to inaccurate kinetic measurement and wrong assignment of mechanisms.[5]

Another challenge in revealing the true mechanism from the conventional ensemble measurement of electrode kinetics is that practical electrode materials often show large heterogeneity.[6-8] Consequently, the measured kinetics is an average over the whole electrode surface, and the detailed distribution of local activity and corresponding mechanisms, including those at hot spots, are inevitably lost during the averaging.[9] Therefore, assigning one mechanism to the whole electrode based on the average kinetic data measured from bulk electrochemical techniques can often be oversimplifying, if not erroneous. To circumvent the issue of heterogeneity, localized electrochemical mapping techniques, including scanning electrochemical cell microscopy (SECCM), has emerged as a powerful technique in assessing local electrochemistry.[10, 11] In SECCM, electrochemical measurement can be confined into a nanoscopic droplet, and the scanning of the droplet on the electrode surface can generate high-resolution maps of local activity. When combined with colocalized imaging techniques, structure and activity can be correlated in a site-by-site manner.[8, 12-14] Despite the great success in mapping the local activity for a range of electrocatalytic reactions and energy storage at the single-particle level,[8, 15-17] the relevance of *iR* drop in the SECCM measurement is often not discussed in detail. While this is warranted when a high concentration of supporting electrolyte is used, the significance of *iR* drop in SECCM setup has rarely been systematically assessed,[18] nor is its compensation method discussed.[19-21] The existence of significant *iR* drop can lead to errors in the determination of local electrocatalytic activity, undermining the great potential of scanning electrochemical probe microscopy in understanding the local electrocatalytic mechanism.

In this paper, we assess the effect of *iR* drop in single-barrel and dual-barrel SECCM voltammetric experiments. In each kind of experiment, we first present the theoretical treatment of *iR* drop, and then validate the theory using finite element simulation and experiments. The theory developed here allows facile and semi-quantitative estimation of the significance of *iR* drop in SECCM measurement. Lastly, we present an experimental method of measuring and compensating *iR* drop in dual-barrel SECCM experiments.

Results and Discussion

1. *iR* drop in single-barrel SECCM.

A schematic for a typical single-barrel SECCM setup is shown in Figure 1a. An electrolyte-filled nanopipette with a nanodroplet at its opening is used as the probe. The active working electrode is defined by the contact between the droplet and the substrate electrode, and a quasi-reference counter electrode (QRCE), often in the form of a wire, is placed inside the pipette barrel. *IR* drop in SECCM experiments is the ohmic potential drop in the solution between the working electrode and the QRCE. In this section, we first derive the analytical expression of the solution resistance in a single-barrel pipette based on an ideal geometry of a truncated cone (Figure 1b). Such an analytical expression helps semi-quantitatively estimate whether *iR* drop is important in the experiment. We then show a more general way to estimate *iR* drop based on the limiting current without the assumption of pipette geometry. Finally, both methods are validated using finite element simulation and applied to experiments.

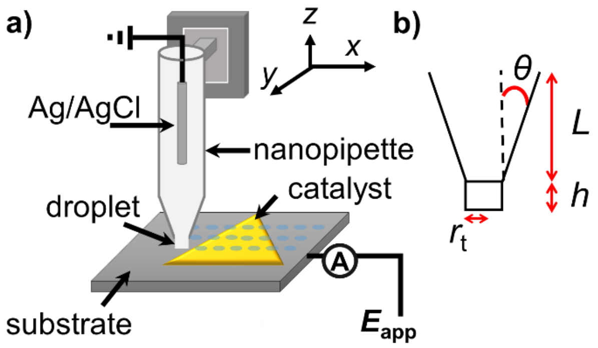

Figure 1. a) Schematic of a single-barrel SECCM setup. b) Ideal cross-sectional geometry of a single-barrel pipette with a cylindrical droplet.

1a. Analytical expression of solution resistance in SECCM

The analytical expression of the solution resistance (R_s) in the single-barrel SECCM is obtained by approximating the geometry of the SECCM probe by a truncated conical nanopipette with a cylindrical droplet as shown in Figure 1b. Accordingly, R_s is composed of droplet resistance (R_d) and the pipette resistance (R_p) in series, which can be expressed as:

$$R_{\mathrm{s}} = R_{\mathrm{d}} + R_{\mathrm{p}} = \int_{-h}^{0} \frac{\mathrm{d}z}{\kappa A} + \int_{0}^{L} \frac{\mathrm{d}z}{\kappa A} \tag{1}$$

In eq 1, κ is the conductivity of the solution, A the cross-section area at the height z, h and L are the height of the droplet and the pipette, respectively, as shown in Figure 1b.

Equation 1 can be simplified assuming a constant κ (detail provided in the ESI section 3), which yields:

$$R_{\mathrm{s}} = R_{\mathrm{d}} + R_{\mathrm{p}} = \frac{h}{\kappa \pi r_{\mathrm{t}}^2} + \frac{L}{\kappa \pi r_{\mathrm{t}}(r_{\mathrm{t}} + L \tan(\theta))} \tag{2}$$

The variables in eq 2 are consistent with those labeled in Figure 1b, where r_t is the pipette tip radius, θ is the half-cone angle, and L is the length of the pipette.

When $L \tan(\theta) \gg r_t$, eq 2 can be further simplified as:

$$R_{\mathrm{s}} = \frac{h}{\kappa \pi r_{\mathrm{t}}^2} + \frac{1}{\kappa \pi r_{\mathrm{t}} \tan(\theta)} \tag{3}$$

To validate the expression of R_s in eq 2, we performed finite element simulation for single-barrel SECCM experiments. Nernst-Planck equation is solved using COMSOL Multiphysics. Electroneutrality is assumed since the thickness of the double layer (i.e., Debye length) when the electrolyte is > 1 mM is negligible when compared with the opening of the pipette in the simulation. The details of the model are provided in the ESI section 3. As shown in Figure 2, the analytical expression of R_s (eq 2) matches very well the simulation results when the half-cone angle (θ) of the nanopipette is smaller than 20°, which is most common in SECCM experiments. The differences between the analytical solution and the finite element results at θ > 20° is explained by the radial diffusion that is not accounted for in the derivation of the eq 2.[22]

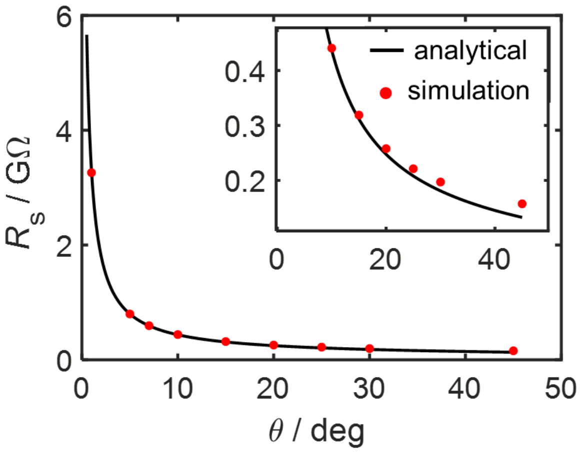

Figure 2. Comparison of the analytical expression (black line, eq 2) and finite element simulation (red dot) of R_s in single-barrel SECCM at various half-cone angles (θ). Inset: zoomed-in portion of the figure between 0 and 0.5 GΩ. The geometry is shown in Figure 1b with h = 350 nm, r_t = 350 nm, L = 1 μm. The solution is 1 mM KCl.

Equation 2 or 3 provides a semi-quantitative way to quickly determine whether *iR* drop in an SECCM experiment is negligible. In practical SECCM experiments, the pipettes are often sufficiently long that eq 2 and eq 3 provide the same result. Under this scenario, R_s can be readily estimated with the knowledge of θ and solution conductivity (κ), which in turn can be calculated based on the solution composition. The *iR* drop is obtained by multiplying R_s with the measured current.

Despite the simplicity, the assumptions in the analytical expression should be noted. First, the eq 2 is derived based on an ideal geometry as drawn in Figure 1b. Although it captures the essence of most single-barrel SECCM experiments, it can be an oversimplification. For more accurate results, one can apply finite element simulation using the exact pipette geometry obtained from TEM as described by Unwin and coworkers.[23] Secondly, a constant conductivity everywhere is assumed when deriving eq 2. However, a change of local solution composition near the electrode surface is generally expected when Faradaic current flows, which alters the local conductivity. Indeed, R_s is never truly constant when Faradaic reactions occur, leading to an over- or under-compensation depending on the exact Faradaic reaction (see section 1c).

1b. Assessing *iR* drop from the limiting current.

An alternative method to assess *iR* drop in single-barrel SECCM without the assumption of pipette geometry is to use the mass transfer limiting current (i_{lim}). The principle is based on the similarity in the mathematical treatment of steady-state mass transport and current conduction: both reduce to Laplace equations, i.e., $\nabla^2 C = 0$ and $\nabla^2 \Phi = 0$, respectively. The i_{lim} for a redox-active species *j* in SECCM can be expressed as:

$$i_{\mathrm{lim}} = GnFD_jC_j^* \tag{4}$$

In this equation, *G* is a geometric factor accounting for the shape of the droplet and the nanopipette, *n* is the number of electrons transferred per one molecule of *j* reacted, *F* is Faraday's constant, D_j and C_j^* are the diffusion coefficient and the bulk concentration of the redox species *j*, respectively.

Similarly, the steady-state ionic current can be expressed as:

$$i = G\kappa\Phi_0 \tag{5}$$

where Φ_0 is the potential difference between the electrode surface and the ground, and κ is the solution conductivity.

By rearranging eq 5, the solution resistance (R_s) is obtained:

$$R_s = \frac{\Phi_0}{i} = \frac{1}{G\kappa} \tag{6}$$

Comparing eqs 4 and 6, solution resistance (R_s) is related to the limiting current (i_{lim}) via:

$$R_s = \frac{1}{G\kappa} = \frac{nFDC^*}{i_{\mathrm{lim}}\,\kappa} \tag{7}$$

Equation 7 is the basis for calculating R_s from the limiting current without the need to know the exact geometry of the droplet or the nanopipette. Because of this, it should apply to other electrochemical systems as well. Since the largest steady-state current for a redox process is measured at i_{lim}, the largest *iR* drop is $i_{\mathrm{lim}}R_s$, which can be readily obtained by rearranging eq 8:

$$i_{\mathrm{lim}}R_s = \frac{nFDC^*}{\kappa} \tag{8}$$

Examples of the largest *iR* drop calculated for various electrolyte compositions using eq 8 are shown in Table 1.

The solution conductivity (κ) could be further calculated using

$$\kappa = F\sum |z_i| u_i C_i = \frac{F^2}{RT}\sum z_i^2 D_i C_i \tag{9}$$

In eq 9, z_i is the charge, u_i the mobility, C_i the concentration, and D_i the diffusional coefficient of the ionic species *i*.

Substituting eq 9 to eq 8 and using *T* = 293 K, one obtains:

$$i_{\mathrm{lim}} R_{\mathrm{s}} = 0.0252 \frac{nD_{\mathrm{redox}} C_{\mathrm{redox}}^*}{\sum z_i^2 D_i C_i} \tag{10}$$

where D_{redox} and C_{redox}^* are the diffusion coefficient and the bulk concentration of the redox species, respectively. Assuming *n* = 1, and a 1:1 electrolyte, eq is further simplified as:

$$i_{\mathrm{lim}} R_{\mathrm{s}} = 0.0252 \frac{D_{\mathrm{redox}} C_{\mathrm{redox}}^*}{\sum D_i C_i} \tag{11}$$

Equation 11 suggests that the maximum *iR* drop is 25 mV times the ratio between the product of *DC* for the redox species over the sum of the product of *DC* for all the ions when n = 1 and 1:1 electrolyte is used.

Table 1. Calculated maximum *iR* drop in different solutions.

Redox Specie	Electrolyte	κ (S/cm)	$i_{\mathrm{lim}} R_{\mathrm{s}}$ (mV)
100 mM $HClO_4$	1 mM KCl	4.26×10^{-2}	21.1
100 mM $HClO_4$	1 mM KCl + 100 mM KNO_3	5.73×10^{-2}	15.7
5 mM $Ru(NH_3)_6Cl_3$	1 mM KNO_3	2.85×10^{-3}	1.5
5 mM $Ru(NH_3)_6Cl_3$	10 mM KNO_3	4.18×10^{-3}	1.0
5 mM ferrocene	1.5 mM $TBAPF_6$	6.88×10^{-5}	21.0
5 mM ferrocene	50 mM $TBAPF_6$	2.29×10^{-3}	0.6
Reduction of H_2O	100 mM KCl	4.26×10^{-2}	2.7×10^{4} *

* assuming 55.5 M of H_2O and the limiting current for water reduction (hydrogen evolution reaction) can be achieved.

1c. Validation using simulation and experiments.

We use finite element simulation to validate the two analytical methods of *iR* drop estimation/correction in single-barrel SECCM (eqs 2 and 7). Three example systems were used, including the oxidation of ferrocene (Fc), the reduction of proton, and the reduction of $\mathrm{Ru(NH_3)_6^{3+}}$. Briefly, both the ideal *iR*-free and the uncorrected raw voltammograms can be simulated numerically. Equation 2 or 7 can then be used to correct the electrode potential in the uncorrected voltammogram using:

$$E_{\mathrm{corr}} = E_{\mathrm{app}} - iR_{\mathrm{s}} \tag{12}$$

where E_{corr} is the *iR*-corrected potential, E_{app} is the applied uncorrected potential, i is the voltammetric current, and R_{s} is the solution resistance calculated using eq 2 or eq 7. Using Fc oxidation as an example, the corrected voltammogram using either eq 2 or eq 7 agrees relatively well with the ideal *iR*-free one as shown in Figure 3a. We do notice an overcompensation at when the voltammetric current is high. To reveal any small errors, we also directly compared R_{s} obtained using eq 2 and eq 7 with that from the simulation. As shown in Figure 3b, both eq 2 and eq 7 predict very similar R_{s} values that are close to the simulation between 0 and 0.3 V, where the Faradaic current is low. At potential >0.3 V where Fc oxidation results in significant Faradaic current, the simulated R_{s} decreases, while eq 2 or 7 predicts a constant R_{s}. A decrease in R_{s} during Fc oxidation is expected because the neutral Fc is converted to an ionic species, ferrocenium ($\mathrm{Fc^+}$), and its accumulation at the electrode surface increases the local conductivity. This change of the local conductivity during the voltammetry is captured in the simulation as shown in Figure 3c-d. The fact that eq 2 or 7 does not capture any change in R_{s} is also not surprising because both equations assume a constant κ during their derivation for simplicity. In principle, a location dependent κ (as shown in Figure 3c-d) should be used when deriving these analytical expressions, however, the mathematical treatment becomes tedious, and the complicated final expression of R_{s} will defeat the purpose of being a simple method to estimate the *iR* drop and therefore is not pursued here. The validation of *iR* drop compensation using the reduction of $\mathrm{H^+}$ and $\mathrm{Ru(NH_3)_6^{3+}}$ as examples are shown in section 5 of the SI. In both cases, the analytical expression provides a relatively accurate estimation of R_s, although it does not capture the change of R_s during the voltammetry. An increase in R_s is expected during proton reduction and $\mathrm{Ru(NH_3)_6^{3+}}$ reduction because the net charge on the redox species decreases after the reduction, which are captured in the finite element simulation as shown in Figures S5 and S6. For $\mathrm{Ru(NH_3)_6^{3+}}$ and proton reduction, a small discrepancy in R_s is observed between eq 2 and eq 7, which is likely due to the ignorance of migration current when deriving eq 7 as discussed in ESI section 5a. Nonetheless, the analytical expressions are very convenient to use, and the error is generally small. We will show in the next section that the subtle change in the solution resistance can be captured experimentally using dual-barrel SECCM setup.

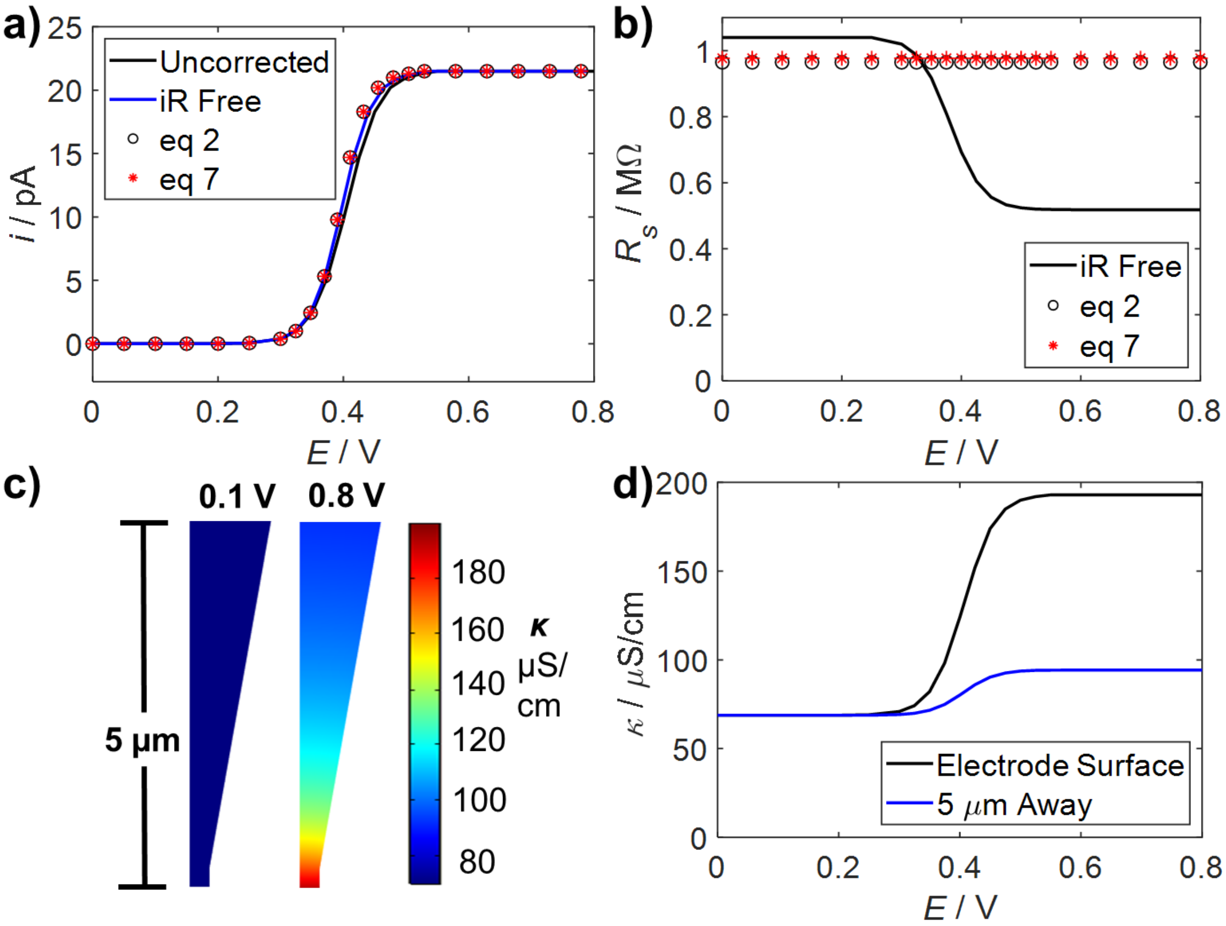

Figure 3. Simulated result of 5 mM Fc in 1.5 mM $\mathrm{TBAPF_6}$. a) Steady-state voltammogram with uncorrected (black), *iR*-free (blue), and corrections by eq 2 (black circle) and eq 7 (red star). b) Solution resistance during the voltammetry. c) Solution conductivity profiles

at the electrode surface up to a distance of 5 μm along the pipette. d) Solution conductivity plots as a function of the applied potential at the electrode surface and at 5 μm along the axisymmetric line.

We further apply the analytical *iR* estimation/compensation methods to experiments. Voltammograms were obtained in the SECCM for Fc oxidation at two concentrations of supporting electrolyte (tetrabutylammonium hexafluorophosphate, $TBAPF_6$) as shown in Figure 4. Qualitatively, the voltammogram with 1.5 mM $TBAPF_6$ shows a larger *iR* drop than the one with 50 mM $TBAPF_6$. To quantify the effect of *iR* drop on the voltammogram, we use the difference of the potentials at 75% and 25% of the limiting current (i.e., $\Delta E = E_{3/4} - E_{1/4}$) to measure the steepness of the rise of the voltammetric wave. A ΔE of 62 mV is observed for the solution with 1.5 mM $TBAPF_6$, and 54 mV for 50 mM $TBAPF_6$ (Figure 4). The solution resistance is calculated based on the solution conductivity and the nanopipette geometry. Using $\theta = 10°$ and and $r_t = 315$ nm, eq 2 predicts a solution resistance of 960 and 29 MΩ for 1.5 mM and 50 mM $TBAPF_6$, respectively. Therefore, the voltammograms with low $TBAPF_6$ display a noticeable *iR* compensation, while the one with high $TBAPF_6$ shows little difference between the corrected and uncorrected voltammograms. After the correction, voltammograms at two different concentrations of $TBAPF_6$ are very similar, with ΔE of 47 mV and 50 mV for 1.5 mM and 50 mM $TBAPF_6$, respectively. The compensation using eq 7 yield very similar results compared to eq 2 and therefore is not shown here. Another experimental example for *iR* compensation in proton reduction reaction is shown in the section 4 of the SI.

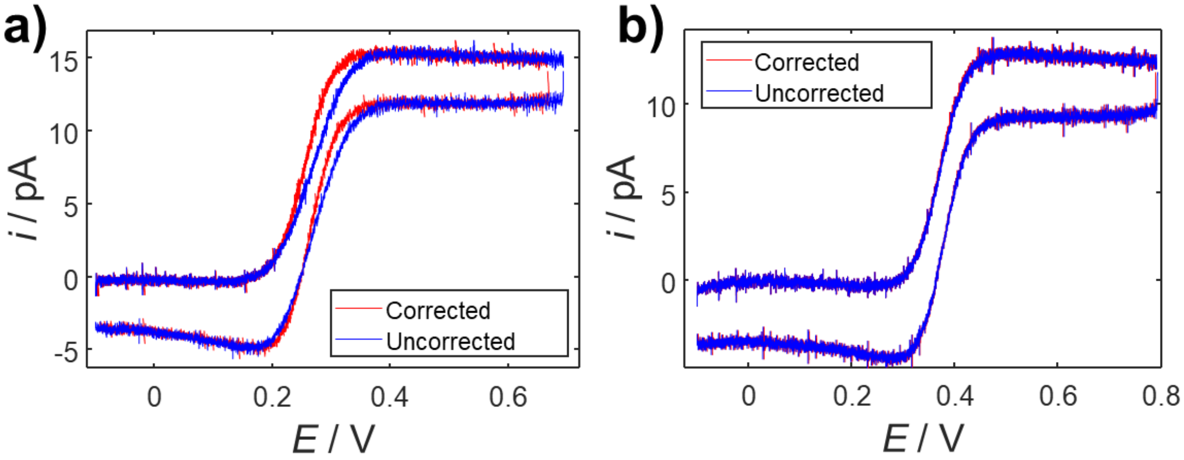

Figure 4. Experimental single-barrel SECCM voltammograms for 5 mM Fc oxidation in propylene carbonate containing a) 1.5 mM and b) 50 mM $TBAPF_6$. Blue: raw uncorrected voltammogram. Red: *iR*-corrected voltammogram using the calculated R_s from eq 2.

2. *iR* drop in dual-barrel SECCM.

2a. General model

Dual-barrel nanopipettes (also known as theta pipettes) have also been used in SECCM for electrochemical mapping, especially when the droplet needs to be scanned over a surface without breaking the contact.[10] The schematic of a dual-barrel setup is shown in Figure 5.

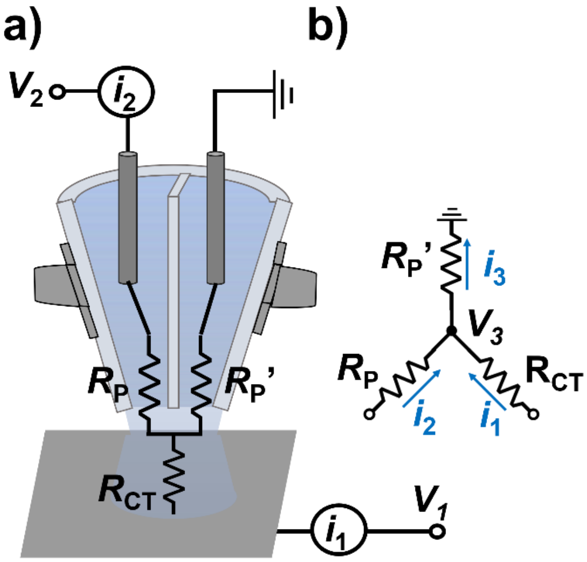

Figure 5. a) Schematic of the dual-barrel SECCM setup. b) an equivalent circuit model.

The major difference between the dual- and single-barrel SECCM is that two QRCEs are used in the dual-barrel setup, each resides in one of the barrels. One way of electrical connection is shown in Figure 5a: potentials of V_1 and V_2 are applied to the working electrode and one QRCE, respectively, with the other QRCE as the ground (right barrel in Figure 5a). The current flowing through the working electrode is recorded as i_1 by a current follower and the current flowing through the QRCE on the left is recorded as i_2. The potential bias V_2 and the current i_2 offer a handle for assessing the solution resistance. Note that i_2 is considered to mostly reflect the ionic current flowing between the pipette barrels, and has been used as a feedback mechanism to maintain a consistent droplet contact at the electrode surface during SECCM.[18] On the other hand, V_2 also causes a shift of the working electrode potential away from V_1,[10] but can be corrected as discussed below.

An equivalent circuit diagram for a dual-barrel SECCM experiment is shown in Figure 5b. Each barrel has a pipette solution resistance (R_{pip} or R_{pip}'). A charge transfer resistance (R_{CT}) governed by the kinetics of the Faradaic reaction is in series with the pipette resistance. The circuit does not include capacitors (e.g., double-layer capacitor) because their contribution is negligible at the steady state. From the circuit in Figure 5b, it is observed that:

$$i_1 + i_2 = i_3 \tag{13}$$

$$V_1 - V_3 = i_1 R_{\mathrm{CT}} \tag{14}$$

$$V_2 - V_3 = i_2 R_P \tag{15}$$

$$V_3 = i_3 R_P' \tag{16}$$

Assuming a symmetrical pipette geometry and therefore $R_P = R_P'$, we obtain:

$$R_P = \frac{V_2}{i_1 + 2i_2} \tag{17}$$

$$R_{\mathrm{CT}} = \frac{i_1(V_1 - V_2) + i_2(2V_1 - V_2)}{i_1^2 + 2i_1 i_2} \tag{18}$$

The potential on the working electrode/electrolyte interface without *iR* drop is then expressed as:

$$V_{\mathrm{WE}} = i_1 R_{CT} = V_1 - \frac{V_2(i_1 + i_2)}{(i_1 + 2i_2)} \tag{19}$$

And the *iR* drop between the working electrode and the QRCE at the ground is:

$$V_{\mathrm{ir}} = \frac{V_2(i_1 + i_2)}{(i_1 + 2i_2)} \tag{20}$$

Equations 19 and 20 are important because V_{WE} represents the electrode potential without *iR* drop. In other words, *iR* corrected voltammogram can be calculated from V_1, V_2, and the measured i_1 and i_2 using eq 19.

When the solution contains excess supporting electrolyte, i.e., $R_p \ll R_{\mathrm{CT}}$, or equivalently when the Faradaic current from the working electrode (i_1) is very small compared to the ionic current, i.e., $i_1 \ll i_2$, eq 19 can be simplified as:

$$V_{\mathrm{WE}} = V_1 - \frac{1}{2}V_2 \tag{21}$$

This suggests that working electrode potential is shifted away from V_1 by $\frac{1}{2}V_2$, consistent with an expression that has been used by Unwin and co-authors.[18] Note that in Unwin's work, the working electrode is connected as the ground. However, the method of *iR* compensation we derived here works regardless of the connection as long as one keeps track of the direction of current flow and therefore will not be discussed here.

2b. Validation using finite element simulation.

The expression for *iR* compensation in dual-barrel SECCM is validated by finite element simulation. We solve the Nernst-Planck equation in 3-D using via COMSOL Multiphysics. The model is described in ESI section 5. The simulated *iR*-free and *iR*-uncorrected voltammograms for the oxidation of 20 mM $\mathrm{Ru(NH_3)_6^{3+}}$ in 1 mM KNO_3 at a potential bias (V_2) of 0.05 V are shown in Figure 6. The uncorrected voltammogram is *iR* compensated using eq 19, and the compensated voltammogram is then compared with the simulated *iR*-free voltammogram. As shown in Figure 6, equation 19 sufficiently compensate the *iR* drop in the voltammogram. The *iR* compensation is not affected by the potential bias as shown by the simulation and validation in Figure S8. Additional cross-sectional potential profiles and voltammogram simulations at various supporting electrolyte concentrations can be found in ESI section 5b.

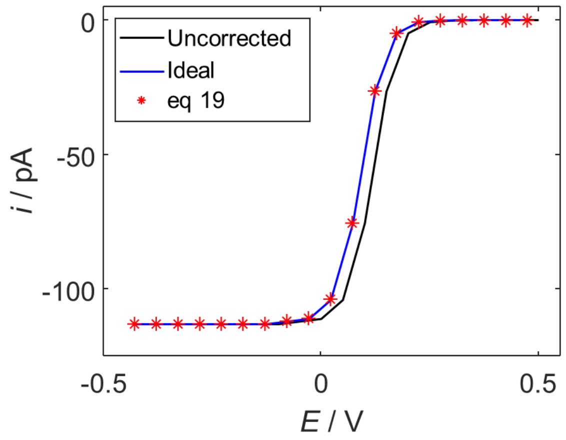

Figure 6. Simulated steady-state uncorrected (black) and ideal *iR*-free (blue) voltammograms of 20 mM $\mathrm{Ru(NH_3)_6^{3+}}$ with 1 mM KNO_3 in a dual-barrel pipette. V_2 =

0.05 V is applied between the two QRCEs. Equation 19 is applied to correct the raw voltammogram for *iR* drop, and the corrected voltammogram is shown as red stars.

2c. Application of *iR* compensation in dual-barrel SECCM experiments.

We now apply the *iR* compensation method to dual-barrel SECCM experiments in three model systems: the oxidation of Fc, the reduction of $\mathrm{Ru(NH_3)_6^{3+}}$ and the reduction of proton. We start the oxidation of 20 mM Fc with different concentrations of $TBAPF_6$. At 1 mM $TBAPF_6$, significant *iR* drop is observed (Figure 7a). This is expected for such a low concentration of supporting electrolyte, and *iR* drop 126 mV is calculated using eq 9 when it is a single-barrel system. When the solution is more conductive at 5 mM and 10 mM $TBAPF_6$, *iR* drop is indeed much smaller as shown by a shaper increase of the voltammetric current (Figure 7a). The *iR* drop can be mostly compensated using eq 19 at all different concentrations of $TBAPF_6$, as shown by the convergence of the corrected voltammograms at different concentrations of $TBAPF_6$ as shown in Figure 7b.

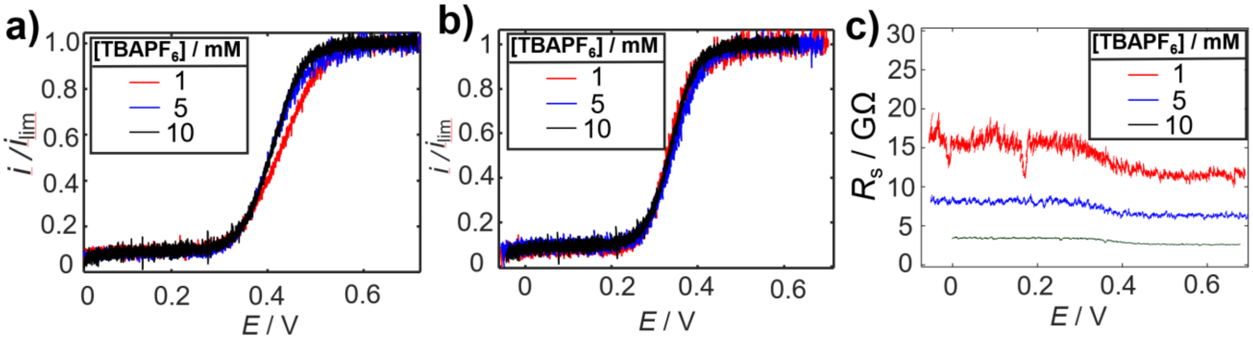

Figure 7. Normalized dual-barrel SECCM voltammograms of 20 mM Fc in propylene carbonate at various concentrations of $TBAPF_6$ a) before and b) after iR correction using eq 19. c) Calculated solution resistance (R_S) from eq. 17 as a function of electrode potential. The substrate is Pt with V_2 = 0.1 V.

The derived *iR* compensation method for dual barrel pipette also allows us to measure R_s during the voltammetry using eq 17. As shown in Figure 7c, the measured R_s overall decreases as the concentrations of the electrolyte increases at all potentials. The same trend is also observed for the reduction of $\mathrm{Ru(NH_3)_6^{3+}}$ and proton as shown in

Figure S5 and S6. For the Fc system at a given electrolyte concentration, a decrease in R_s is observed when the electrode potential is swept more positively to induce the oxidation of Fc as shown in Figure 7c. As discussed previously in section 1c, this is expected as the oxidation of Fc generates the ionic species, Fc^+, and therefore decreases the solution resistance. Our method also successfully captures the change of R_s during voltammetry for other systems, including the reduction of $\mathrm{Ru(NH_3)_6^{3+}}$ and proton. In both systems, an increase in R_s is observed as expected, which are shown in ESI section 6.

Note that to obtain a good *iR* compensation, i_2 needs to be measured accurately, especially when the solution is highly resistant and i_2 is low. Under this scenario, the noise of i_2, as well as any offset and leakage current from the amplifier itself can cause issues in *iR* compensation using eq 19. We refer the readers to section 7 in the ESI for the discussion of noise during *iR* compensation.

Conclusions

We have shown several methods of *iR* drop compensation in SECCM experiments, which are validated using finite element simulation and experiments. In single-barrel SECCM experiments, solution resistance can be estimated based on solution composition and the pipette geometry. A more general method using the limiting current for *iR* compensation is also proposed and validated, which does not assume any specific geometry of the nanopipette, and can be potentially applied to other nanoelectrochemical systems. We also developed a method of directly measuring the solution resistance in dual-barrel SECCM, which also corrects the potential shift in this type of experiment. The methods presented here can provide a fast estimation of the significance of *iR* drop in an SECCM experiment, as well as a method to compensate the *iR* drop. We envision this will allow more accurate local electrode kinetics measurement in SECCM, contributing to the revelation of local structure-dependent electrocatalytic mechanism.

Appendix 1. Common symbols used in this manuscript

We listed below some of the common symbols used throughout the manuscript.

symbol	meaning
V_1	potential applied at the electrode surface
V_2	potential applied between the two QRCEs in the dual-barrel SECCM
i_1	current flowing through the substrate electrode
i_2	current flowing from one pipette to the other under the bias V_2.
R_S	solution resistance
R_p	Solution resistance in one barrel of the dual-barrel pipette
R_{CT}	Charge transfer resistance
i_{lim}	Mass transfer limiting current
V_{WE}	the actual potential at the working electrode without iR drop
V_{ir}	the ohmic potential drop in the solution (i.e., *iR* drop)
G	Geometric factor for the single-barrel pipette
κ	Conductivity of the solution
E	electrode potential
θ	half-cone angle
r_t	tip radius of the pipette

Author Contributions.

§ BB and GJ contribute equally to the work. BB, GJ performed the key experiments and data analysis. GJ performed the simulation. YW characterized the nanopipette. HR conceived the project and draft the manuscript.

Acknowledgments

The research was sponsored by the Defense Advanced Research Project Agency (DARPA) and the Army Research Office and was accomplished under Grant Number W911NF-20-1-0304. The views and conclusions contained in this document are those of the authors and should not be interpreted as representing the official policies, either expressed or implied, of the Defense Advanced Research Project Agency (DARPA) and the Army Research Office or the U.S. Government. The U.S. Government is authorized to reproduce and distribute reprints for Government purposes notwithstanding any copyright notation herein. Acknowledgment is made to the Donors of the American Chemical Society Petroleum Research Fund for partial support of this research. We thank Dr. Kim McKelvey for the help in the WEC-SPM software.

Notes

Electronic Supplementary Information (ESI) available: Experimental methods, pipette characterization, derivation of solution resistance, additional results in single-barrel SECCM, finite element simulation, measuring solution resistance in dual-barrel SECCM, effect of noise.

References

1. Z. Yang, J. Zhang, M. C. W. Kintner-Meyer, X. Lu, D. Choi, J. P. Lemmon and J. Liu, *Chem. Rev.*, 2011, **111**, 3577-3613.
2. S. P. S. Badwal, S. S. Giddey, C. Munnings, A. I. Bhatt and A. F. Hollenkamp, *Frontiers in Chemistry*, 2014, **2**.
3. T. Shinagawa, A. T. Garcia-Esparza and K. Takanabe, *Scientific Reports*, 2015, **5**, 13801.
4. A. J. Bard and L. R. Faulkner, *Electrochemical methods : fundamentals and applications*, Wiley, New York, 1980.
5. G. Marcandalli, A. Goyal and M. T. M. Koper, *ACS Catal.*, 2021, **11**, 4936-4945.
6. C. L. Bentley, M. Kang and P. R. Unwin, *Journal of the American Chemical Society*, 2019, **141**, 2179-2193.
7. M. J. S. Farias, W. Cheuquepan, G. A. Camara and J. M. Feliu, *ACS Catal.*, 2016, **6**, 2997-3007.
8. C. L. Bentley, M. Kang, F. M. Maddar, F. Li, M. Walker, J. Zhang and P. R. Unwin, *Chem. Sci.*, 2017, **8**, 6583-6593.
9. Y.-L. Ying, J. Wang, A. R. Leach, Y. Jiang, R. Gao, C. Xu, M. Edwards, A. D. Pendergast, H. Ren, K. T. Weatherly Connor, W. Wang, P. Actis, L. Mao, H. S. White and Y.-T. Long, *SCIENCE CHINA Chemistry*, 2020, **63**, 1674-7291.

10. N. Ebejer, M. Schnippering, A. W. Colburn, M. A. Edwards and P. R. Unwin, *Anal. Chem.*, 2010, **82**, 9141-9145.

11. L. C. Yule, C. L. Bentley, G. West, B. A. Shollock and P. R. Unwin, *Electrochim. Acta*, 2019, **298**, 80-88.

12. E. Daviddi, K. L. Gonos, A. W. Colburn, C. L. Bentley and P. R. Unwin, *Anal. Chem.*, 2019, **91**, 9229-9237.

13. R. G. Mariano, M. Kang, O. J. Wahab, I. J. McPherson, J. A. Rabinowitz, P. R. Unwin and M. W. Kanan, *Nat. Mater.*, 2021, **20**, 1000-1006.

14. J. T. Mefford, A. R. Akbashev, M. Kang, C. L. Bentley, W. E. Gent, H. D. Deng, D. H. Alsem, Y.-S. Yu, N. J. Salmon, D. A. Shapiro, P. R. Unwin and W. C. Chueh, *Nature*, 2021, **593**, 67-73.

15. A. Kumatani, C. Miura, H. Kuramochi, T. Ohto, M. Wakisaka, Y. Nagata, H. Ida, Y. Takahashi, K. Hu, S. Jeong, J.-i. Fujita, T. Matsue and Y. Ito, *Advanced Science*, 2019, **6**, 1900119.

16. Y. Takahashi, A. Kumatani, H. Munakata, H. Inomata, K. Ito, K. Ino, H. Shiku, P. R. Unwin, Y. E. Korchev, K. Kanamura and T. Matsue, *Nat. Commun.*, 2014, **5**, 5450.

17. R. G. Mariano, K. McKelvey, H. S. White and M. W. Kanan, *Science*, 2017, **358**, 1187-1192.

18. M. E. Snowden, A. G. Güell, S. C. S. Lai, K. McKelvey, N. Ebejer, M. A. O'Connell, A. W. Colburn and P. R. Unwin, *Anal. Chem.*, 2012, **84**, 2483-2491.

19. B. Tao, L. C. Yule, E. Daviddi, C. L. Bentley and P. R. Unwin, *Angew. Chem. Int. Ed.*, 2019, **58**, 4606-4611.

20. B. D. B. Aaronson, S. C. S. Lai and P. R. Unwin, *Langmuir*, 2014, **30**, 1915-1919.

21. S.-y. Tan, P. R. Unwin, J. V. Macpherson, J. Zhang and A. M. Bond, *Anal. Chem.*, 2017, **89**, 2830-2837.

22. B. Zhang, Y. Zhang and H. S. White, *Anal. Chem.*, 2006, **78**, 477-483.

23. D. Perry, D. Momotenko, R. A. Lazenby, M. Kang and P. R. Unwin, *Anal. Chem.*, 2016, **88**, 5523-5530.